




## Surface morphological characterization of activated carbon-metal (hydr)oxide composites: some insights into the role of the precursor chemistry in aqueous solution

Adrián Barroso-Bogeat, María Alexandre-Franco, Carmen Fernández-González & Vicente Gómez-Serrano


To cite this article: Adrián Barroso-Bogeat, María Alexandre-Franco, Carmen Fernández-González & Vicente Gómez-Serrano (2020) Surface morphological characterization of activated carbon-metal (hydr)oxide composites: some insights into the role of the precursor chemistry in aqueous solution, Journal of Dispersion Science and Technology, 41:12, 1743-1753, DOI: [10.1080/01932691.2019.1635889](https://doi.org/10.1080/01932691.2019.1635889)


To link to this article: <https://doi.org/10.1080/01932691.2019.1635889>

 View supplementary material [↗](#)

 Published online: 09 Jul 2019.

 Submit your article to this journal [↗](#)

 Article views: 25


 View related articles [↗](#)

 View Crossmark data [↗](#)

 Citing articles: 1 View citing articles [↗](#)



## Surface morphological characterization of activated carbon-metal (hydr)oxide composites: some insights into the role of the precursor chemistry in aqueous solution

Adrián Barroso-Bogeat<sup>a,b</sup> , María Alexandre-Franco<sup>c</sup>, Carmen Fernández-González<sup>c</sup>, and Vicente Gómez-Serrano<sup>c</sup>

<sup>a</sup>Departamento de Ciencia de los Materiales e Ingeniería Metalúrgica y Química Inorgánica, Universidad de Cádiz, Puerto Real (Cádiz), Spain;

<sup>b</sup>Instituto de Investigación en Microscopía Electrónica y Materiales (IMEYMAT), Universidad de Cádiz, Puerto Real (Cádiz), Spain;

<sup>c</sup>Departamento de Química Orgánica e Inorgánica, Universidad de Extremadura, Badajoz, Spain

### ABSTRACT

Morphological features of metal (hydr)oxide (MO) particles supported on activated carbon (AC) largely influence the performance of these composite materials in most of their applications, particularly in heterogeneous catalysis. Furthermore, the MO precursor as well as the preparation method and conditions strongly determine these morphological features. Thus, the present work is aimed at shedding light on the role of the precursor chemistry on the surface morphology of a series of AC-MO composites prepared by wet impregnation of a commercial AC with  $\text{Al}(\text{NO}_3)_3$ ,  $\text{Fe}(\text{NO}_3)_3$ , and  $\text{Zn}(\text{NO}_3)_2$  in aqueous solution. These materials are characterized by X-ray diffraction, scanning electron microscopy and energy dispersive X-ray spectroscopy. The microstructure, morphology, size distribution and degree of dispersion of the supported MO (nano)particles strongly depend on the chemical transformations undergone by the precursors not only in the impregnation solutions after their contact with AC but also during the oven-drying step.  $\text{Al}^{3+}$ ,  $\text{Fe}^{3+}$  and  $\text{Zn}^{2+}$  species in aqueous medium are involved in hydrolysis and polymerization processes, which notably modify the pH of the starting precursor solutions. Upon their contact with AC, pH markedly increases due to the strong basic character of the carbon surface ( $\text{pH}_{\text{pzc}} \approx 10.50$ ), leading to the precipitation of the metal hydroxides or oxyhydroxides. Both supported bayerite ( $\alpha\text{-Al}(\text{OH})_3$ ) and goethite ( $\alpha\text{-FeO}(\text{OH})$ ) are essentially amorphous; however, the former grows in micrometric particles while the latter does as nanoparticles. By contrast, the higher crystallinity and larger particle size of supported wülfingite ( $\varepsilon\text{-Zn}(\text{OH})_2$ ) are connected with an additional transformation of the as-precipitated amorphous hydroxide during the heating step at  $120^\circ\text{C}$ .

### ARTICLE HISTORY

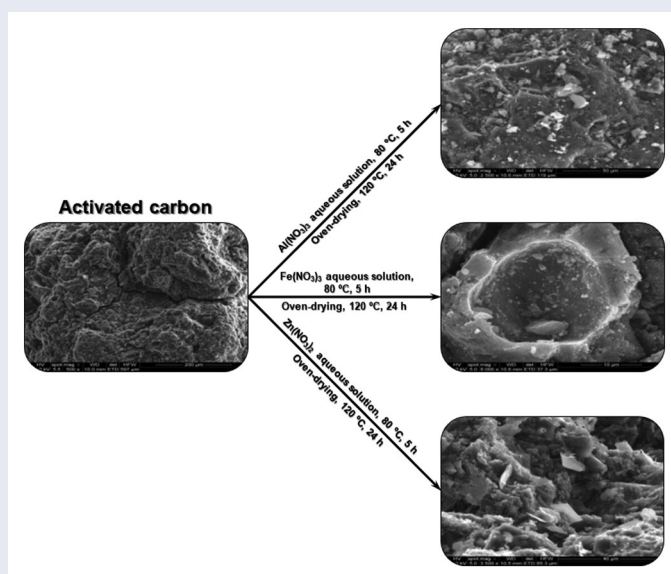
Received 8 February 2019



Accepted 15 June 2019


### KEYWORDS

Activated carbon; aqueous solution; metal (hydr)oxides; precursor chemistry; surface characterization

### GRAPHICAL ABSTRACT



**CONTACT** Adrián Barroso-Bogeat  [adrian.barroso@uca.es](mailto:adrian.barroso@uca.es)  Departamento de Ciencia de los Materiales e Ingeniería Metalúrgica y Química Inorgánica, Universidad de Cádiz, Campus Río San Pedro s/n, 11510 Puerto Real (Cádiz), Spain.

 Supplemental data for this article can be accessed on the [publisher's website](#).

## Introduction

Over the last decades, novel composites comprising (nano)-particles of metal oxides and/or hydroxides (henceforth referred to as MOs) supported on activated carbon (AC, hereafter) have received a great deal of attention owing to their set of applications in a variety of fields, such as heterogeneous catalysis, photocatalysis, adsorption of organic and inorganic pollutants both in gas and liquid streams, energy storage devices, and so on.<sup>[1]</sup> AC has been long selected as a support of metal-containing (nano)particles due to a number of excellent and unique properties, which have been extensively discussed and comprehensively reviewed in the literature.<sup>[2–8]</sup> Supported metal phases include not only oxides, such as TiO<sub>2</sub>, Fe<sub>2</sub>O<sub>3</sub>, Fe<sub>3</sub>O<sub>4</sub>, ZnO, WO<sub>3</sub> and SnO<sub>2</sub>, but also some hydroxides and oxyhydroxides like bayerite ( $\alpha$ -Al(OH)<sub>3</sub>), goethite ( $\alpha$ -FeO(OH)), wülfingite ( $\epsilon$ -Zn(OH)<sub>2</sub>), Co(OH)<sub>2</sub> and Ni(OH)<sub>2</sub>. In this connection, a detailed and critical review on the preparation methods and applications of several MOs supported on AC has been reported elsewhere.<sup>[9]</sup>

It is well-established that the morphological features, especially the shape, size distribution, crystalline or amorphous nature, crystalline habit, exposed facets, homogeneity and degree of dispersion of the supported (nano)particles strongly influence the behavior and performance of these AC-MO composites in most of their practical applications. Concerning their use as heterogeneous catalysts, although the catalytic activity is determined to a large extent by the chemical composition and properties of the active phase, a high degree of dispersion of the MO (nano)particles enhances the catalytic efficiency in a significant manner.<sup>[4]</sup> In this regard, note that AC is frequently selected as a catalyst support chiefly because of its large surface area and well-developed porosity, which allow preparing supported catalysts with a good dispersion of the active phase and thereby increase its resistance to sintering when operating at elevated temperatures under reaction conditions.<sup>[2–8,10–13]</sup> Furthermore, the presence of a variety of chemical functional groups and structures on AC surface, especially those containing oxygen, improves the dispersion of the active phase, as they can provide anchorage sites or nucleation centers for the precursor during the adsorption, impregnation or precipitation-deposition stage in the preparation of the catalyst, thus controlling both the size and shape of the supported catalytic (nano)particles.<sup>[14–19]</sup> These surface functionalities markedly decrease the hydrophobic character of the carbon surface and make it more accessible to the aqueous solution of the precursor.<sup>[20–24]</sup> On the other hand, recent advances in nanoscience and nanotechnology have allowed the rational design and synthesis of highly efficient catalysts by means of precise control of (nano)particles' composition, morphology, structure and electronic states. For example, by tuning the morphology of catalysts at the nanoscale it is possible to quantitatively design and preferentially expose those crystal facets which are highly active, thereby increasing the surface density of active sites and the overall catalytic efficiency.<sup>[25]</sup> Finally, several studies have suggested a dependence of the catalytic activity on the shape

of the size distribution for supported catalysts.<sup>[26–32]</sup> Therefore, it becomes apparent the need of estimating not only the average particle and/or crystallite size, but even more importantly the size distribution.<sup>[33,34]</sup>

On the other hand, it is also agreed that the MO precursor (e.g. metal nitrate, chloride, acetate, alkoxide, and so on) as well as the preparation method and conditions (i.e. precursor concentration, solvent, temperature, and so forth) largely determine the aforementioned morphological features of supported MO (nano)particles. Notwithstanding, due to its inherent complexity this latter relationship is often ignored or, at best, very poorly investigated and understood. Accordingly, the present work is chiefly intended to gain some additional insight into the role of the precursor chemistry in aqueous solution on the surface morphology of a series of AC-MO composite materials prepared from a commercial AC by wet impregnation with three common MO precursors (Al(NO<sub>3</sub>)<sub>3</sub>, Fe(NO<sub>3</sub>)<sub>3</sub> and Zn(NO<sub>3</sub>)<sub>2</sub>). For such an aim, the surface of the as-prepared hybrid materials is characterized by X-ray diffraction (XRD), scanning electron microscopy (SEM), and energy dispersive X-ray spectroscopy (X-EDS). Obtained surface characterization results are analyzed and interpreted on the basis of the feasible chemical transformations undergone by the metal nitrate precursors during the different preparation steps (i.e. impregnation and oven-drying), with special emphasis on those affecting the composition of the precursor solutions as a result of their contact with the raw carbon support during the impregnation stage.

## Materials and methods

### Materials and reagents

A granular AC purchased from Merck, 1.5 mm average grain size (Cod. 1.02514.1000), as received without any further treatment, was used as support for three MOs. Metal nitrate salts, which are readily soluble in water, were selected as MO precursors. These were Al(NO<sub>3</sub>)<sub>3</sub>·9H<sub>2</sub>O, Fe(NO<sub>3</sub>)<sub>3</sub>·9H<sub>2</sub>O and Zn(NO<sub>3</sub>)<sub>2</sub>·6H<sub>2</sub>O, all of them supplied by Panreac and being of reagent grade.

### Preparation of AC-MO composites

The preparation of the AC-MO composites was performed by the method of wet impregnation in two successive steps

**Table 1.** Preparation of the AC-MO composites: yields and sample codes.

Precursor	pH	Yield/wt.%	Code
Al(NO <sub>3</sub> ) <sub>3</sub> ·9H <sub>2</sub> O	2.91	102	A120
Fe(NO <sub>3</sub> ) <sub>3</sub> ·9H <sub>2</sub> O	1.54	114	F120
Zn(NO <sub>3</sub> ) <sub>2</sub> ·6H <sub>2</sub> O	5.16	103	Z120

**Table 2.** Ash content, crystalline phases, and their mean crystallite size (*D*) for the prepared AC-MO composites.

Sample	Ash content/wt.%	Crystalline phases	<i>D</i> /nm
A120	7.1	Bayerite ( $\alpha$ -Al(OH) <sub>3</sub> )	1.06
F120	13.6	Goethite ( $\alpha$ -FeO(OH))	2.32
Z120	9.7	Wülfingite ( $\epsilon$ -Zn(OH) <sub>2</sub> )	29.90
		Zincite (ZnO)	60.02

of soaking and oven-drying, as previously described in detail elsewhere.<sup>[35–37]</sup> Briefly, about 25 g of AC was impregnated with 250 mL of an aqueous solution of the corresponding MO precursor, using a precursor to AC ratio of 1:1 (w/w). The pH of these freshly prepared solutions was measured immediately before impregnation, and obtained values are set out in Table 1. The impregnation system was placed in a three necked flask and heated at 80 °C under continuous mechanical stirring of 100 rpm for 5 h. Once this time had elapsed, the impregnated products were first vacuum-filtered with the aid of a water pump and then oven-dried at 120 °C for 24 h. The yield of the overall preparation process of the hybrid materials was roughly estimated by the following expression:

$$\text{Yield(wt.\%)} = \frac{M_f(\text{g})}{M_i(\text{g})} \cdot 100 \quad [1]$$

where  $M_i$  is the initial mass of AC and  $M_f$  stands for the final mass of impregnated and oven-dried product. The yield values for the resulting AC-MO hybrid materials are also listed in Table 1, together with the codes assigned to the samples.

### Surface characterization of AC-MO composites

The ash content of the raw AC and the prepared composites was determined by incineration at 650 °C for 12 h in a muffle furnace (Selecta). The obtained results, which may be regarded as rough estimates of the amount of supported MOs, are compiled in Table 2.

The crystalline phases present in each hybrid material were identified by XRD, using a D8 Bruker Advance diffractometer working with Cu K $\alpha$  radiation ( $\lambda = 1.5406 \text{ \AA}$ ). The patterns were collected in the step scanning mode of 0.02° ( $2\theta$ ) and 0.5 s·step<sup>-1</sup> counting time, within the range from 10 to 80°. The mean crystallite size ( $D$ ) for each of the identified phases was estimated by applying the Scherrer equation to their most intense diffraction peaks. These values are also shown in Table 2.

The surface morphology of the prepared AC-MO composites was analyzed by SEM. Images were recorded with a microscope model Quanta 3D FEG (FEI Company) operating in the high vacuum mode under an accelerating voltage ranging from 0.2 to 30 kV, and using an Everhart-Thornley detector for secondary electrons. The sample, as prepared without any further treatment, was mounted onto an aluminum specimen stub with the aid of a conductive carbon adhesive. The microscope was also attached to an energy dispersive X-ray analysis (X-EDS) detector able to estimate the surface elemental composition of the samples under study.

**Table 3.** Number of analyzed micrographs, total number of particles counted and average Feret's diameter for each AC-MO composite.

Sample	Number of micrographs (N)	Total number of particles counted	Average Feret's diameter ( $d_f$ )/nm
A120	4	5100	7472.4
F120	5	14,095	81.7
Z120	4	7056	7991.9

In the present work, a set of at least 12 SEM images in random regions were acquired for each sample at different magnification levels, thus ensuring a minimum quantitative of particles for the estimation of the particle size distribution (PSD) according to the international standard ISO 13322-1.<sup>[38]</sup> Image processing and analysis were carried out by using ImageJ, a free software developed at the National Institute of Health (NIH),<sup>[39]</sup> following the procedure previously described in detail by Mazzoli and Favoni,<sup>[40,41]</sup> with the additional corrections subsequently introduced by Barroso-Bogeat et al.<sup>[42]</sup> In this connection, it is worth noting that the assessment of the PSD in AC-supported MO hybrid materials from SEM images is a very difficult task for several reasons. First, the detection and analysis of small MO aggregates dispersed on AC surface is rather complicated, particularly when the particle size approaches that of phase contrast arising from the support.<sup>[43,44]</sup> Second, this drawback is exacerbated by the fact that the MO particles may be found at different heights, embedded in the carbon support or overlapped by other particles, and because the AC surface is very rough. Therefore, in order to overcome these shortcomings and enhance the visibility of the supported MO particles as much as possible, the intensity of the background was determined and subtracted from the original SEM images. For such an aim, a Gaussian blur filter with a high value for the radius (here, typically 25 pixels) was applied to the original micrograph, thus generating an image of the background. The filtered image was then subtracted from the original one. Finally, the PSD was assessed directly from the resulting background-subtracted image after adjusting its brightness and contrast properly. On the other hand, among the variety of parameters proposed in the literature, Feret's diameter has been considered as the best choice for defining both the shape and size of the MO (nano)particles supported on AC surface. This latter is defined as the longest distance between two parallel tangents on opposite sides of the image particle.<sup>[38]</sup> Table 3 gathers the number of micrographs, the total number of particles counted and the average Feret's diameter value for each composite.

## Results and discussion

### SEM and XRD characterization

#### AC support

First, it is well-known that not only the texture but also the morphology and surface chemistry of activated carbons are strongly dependent on the feedstock and the experimental method followed in their preparation, including both the activating agent and the operational conditions.<sup>[45,46]</sup> Because of the complete lack of knowledge about the raw material and the manufacture process for the commercial AC used in the present work, it becomes clear that meaningful conclusions about the origin of its morphological and surface chemical features cannot be confidently drawn. Figure 1 depicts representative SEM images of the pristine AC at different magnification levels. As can be seen, the AC grains exhibit a very irregular and wrinkled external surface

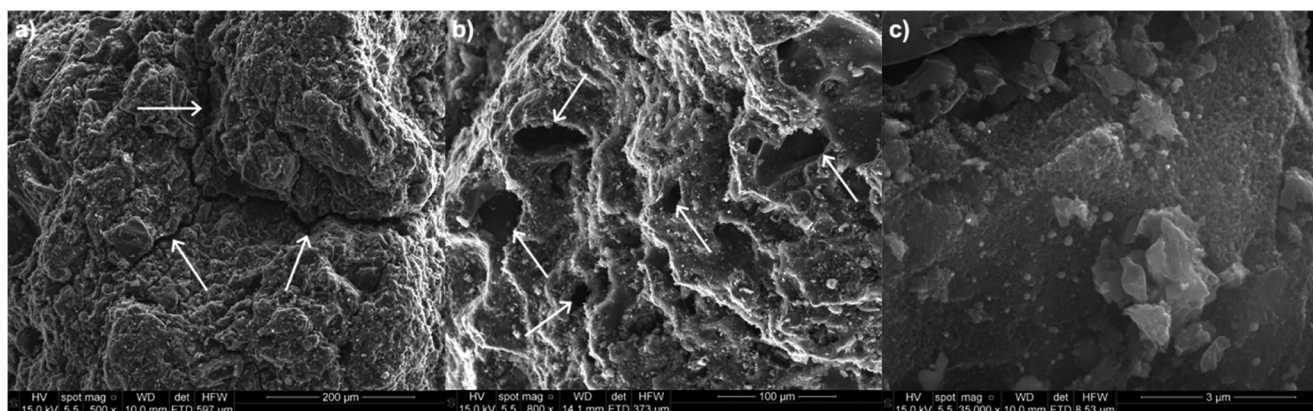


Figure 1. Selected SEM images for the raw AC.

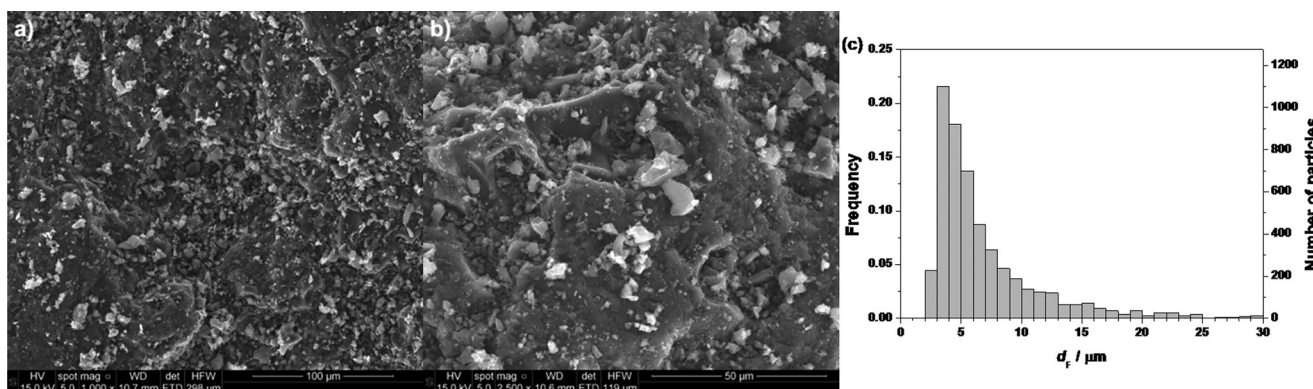


Figure 2. Selected SEM images ((a) and (b)) and PSD (c) for the composite A120.

plenty of cracks, crevices, fissures, and slits (e.g. positions arrowed in Figure 1a), together with smooth open pores of variable sizes (e.g. positions arrowed in Figure 1b). These crevices are considered to be shrinkage cracks either produced during the carbonization of the precursor material<sup>[45,46]</sup> or developed as a result of thermal stresses on the carbon matrix due to temperature changes or gradients in the activation stage.<sup>[47,48]</sup> It is worth noting that at the levels of magnification and resolution used in the present work, most of the pores seen on the micrographs are macropores. A large number of open macropores with variable widths are clearly observed in Figure 1b, thus suggesting AC possesses a well-developed and heterogeneous macroporosity. These observations are in accord with the relatively high macropore volume estimated for this carbon material (i.e.  $V_{\text{ma}} = 0.21 \text{ cm}^3 \cdot \text{g}^{-1}$ ) and its mercury intrusion curve previously reported elsewhere.<sup>[49]</sup> The macropores exhibit entrances with a variety of shapes (ellipsoidal, elongated, round, oblong, and so on) and their distribution over the outer surface of AC appears to be homogeneous and entirely random. As usual for activated carbons, these large pores on the external surface are connected with a whole and extensive network of smaller pores (i.e. meso- and micropores) in the inner of the carbon matrix. Detailed examination of the higher magnification image in Figure 1c shows that, in addition to the aforesaid large size pores, the external surface of AC is highly eroded and also displays numerous holes, similar to pits, with variable dimensions. Finally, the broadly

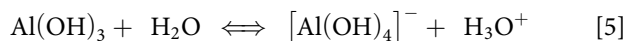
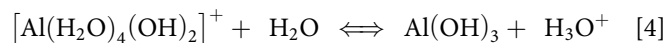
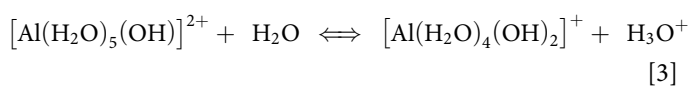
varied porosity observed in Figure 1 reveals the complexity of defining a generalized pore structure for activated carbons, thus questioning the validity of the traditional models such as the slit-shaped model widely used for modeling the adsorption of gases and vapors, or the cylindrical model typically employed by the technique of mercury porosimetry.

On the other hand, the appearance of some brighter spots and small solid structures irregularly dispersed over the outer carbon surface is unambiguously connected with the inorganic fraction of AC and thereby with its ash content, which has been estimated to be around 4.7 wt.%. Such value is markedly lower than those reported for other commercial and lab-made activated carbons, which may contain up to 15 wt.% of mineral matter.<sup>[5]</sup> This inorganic fraction includes all those chemical constituents which either come from the mineral matter in the feedstock,<sup>[50,51]</sup> are present as a result of the activation stage in the preparation process (e.g. phosphorous, potassium, and zinc and chlorine, for activated carbons prepared by chemical activation with phosphoric acid, potassium hydroxide and zinc chloride, respectively), or are deposited on the carbon surface as products of surface reactions.<sup>[52]</sup> As identified from XRD analysis, ashes are mainly composed of mullite ( $\text{Al}_{4.64}\text{Si}_{1.36}\text{O}_{9.68}$ ) and  $\text{SiO}_2$ .

#### AC-MO composites

**A120.** Some representative SEM micrographs of the hybrid material A120 are illustrated in Figure 2. By comparing

these images to those registered for the raw carbon substrate (see Figure 1), it becomes clear that the external surface of A120 is much coarser due to the deposition of a very large number of brighter particles as a result of the impregnation treatment of AC with  $\text{Al}(\text{NO}_3)_3$  aqueous solution and the subsequent oven-drying step at  $120^\circ\text{C}$ . A higher magnification micrograph in Figure 2b reveals that such particles as a rule are very irregularly shaped and distributed over the outer surface of AC. As far as the size of the supported particles is concerned, at first sight one observes that they exhibit a great variety of dimensions, ranging from some hundreds of nanometers up to several tens of micrometres, with predominance of those having a few micrometres. Such observations are well in agreement with the PSD obtained for sample A120 by image processing and plotted in Figure 2c. This histogram shows a very broad distribution of sizes with a long tail to the right up to  $30\ \mu\text{m}$  and most particles (i.e. around 85%) below  $10\ \mu\text{m}$  in size; the average Feret's diameter is estimated to be  $7.5\ \mu\text{m}$ . According to the XRD pattern for A120 (see Figure S1), bayerite ( $\alpha\text{-Al}(\text{OH})_3$ , monoclinic system, space group  $P2_1/a$ ) has been identified as the single constituent of the particles supported on AC. Bayerite grows with a very poor degree of crystallinity, as evidenced from the fact that its mean crystalline domain size was below the detection limit of the technique. Therefore, it is evident that the brighter particles dispersed all over the darker external surface of AC as seen in Figure 2a and b are amorphous entities consisting of aggregates of a very large number of tiny, nanometre-sized, bayerite crystallites. Anyway, it should be noted that the hourglass and semi-hourglass shaped microcrystals characteristic of bayerite, named somatoids,<sup>[53]</sup> are not detected at the magnification levels applied in the present work, which corroborates the essentially amorphous nature of the supported  $\text{Al}(\text{OH})_3$ . The deposition of bayerite on AC surface upon the preparation process of A120 may be explained in the following way. As the pH of the point of zero charge ( $\text{pH}_{\text{pzc}}$ ) is as high as 10.50 for AC,<sup>[54]</sup> pH of the impregnation  $\text{Al}(\text{NO}_3)_3$  aqueous solution (initial  $\text{pH} \approx 2.91$ ) should increase after contact is established due to the protonation of basal plane sites on carbon made up of both oxygen-free type sites and pyrone type sites.<sup>[55]</sup> Such an increase in the pH of the impregnation solution should markedly influence on the hydrolysis processes involving  $\text{Al}^{3+}$  chemical species, thus leading to the formation of hydrolytic species other than those found in the starting solution. With increasing pH and depending on concentration, the following mononuclear  $\text{Al}^{3+}$  species in aqueous solution have been reported: (i)  $[\text{Al}(\text{H}_2\text{O})_6]^{3+}$ , (ii)  $[\text{Al}(\text{H}_2\text{O})_5(\text{OH})]^{2+}$ ,  $[\text{Al}(\text{H}_2\text{O})_4(\text{OH})_2]^+$  and colloidal  $\text{Al}(\text{OH})_3$ , and (iii)  $[\text{Al}(\text{OH})_4]^-$  or  $\text{AlO}_2^-$ , which are all connected by this simple four-stage equilibrium reaction:<sup>[56–59]</sup>



Furthermore, the presence of polynuclear hydrolytic species in aqueous solution showing the general formula  $[\text{Al}_p(\text{OH})_q]^{(3p-q)+}$  and high molecular mass should also be borne in mind owing to the high tendency of  $\text{Al}^{3+}$  to polymerize.<sup>[57,59]</sup> Among the variety of proposed polynuclear species, those having strong experimental evidence are  $[\text{Al}_2(\text{OH})_2]^{4+}$ ,  $[\text{Al}_2(\text{OH})_5]^+$ ,  $[\text{Al}_3(\text{OH})_8]^+$ ,  $[\text{Al}_3(\text{OH})_4]^{5+}$ ,  $[\text{Al}_6(\text{OH})_{20}(\text{H}_2\text{O})_x]^{4+}$ ,  $[\text{Al}_6(\text{OH})_{12}(\text{H}_2\text{O})_{12}]^{6+}$  and  $[\text{Al}_{54}(\text{OH})_{144}(\text{H}_2\text{O})_{36}]^{18+}$ .<sup>[56]</sup> In this connection, it has been reported that temperature markedly affects the solubility, hydrolysis, polymerization and molecular mass distribution of  $\text{Al}^{3+}$  species in aqueous solution.<sup>[58]</sup> Thus, for the impregnation solution the extent of the  $\text{Al}^{3+}$  hydrolysis and polymerization processes, and thereby the amount of high molecular mass species, are expected to be much greater at  $80^\circ\text{C}$  as compared to those observed at room temperature. This fact, together with the relatively high  $\text{Al}^{3+}$  concentration (i.e. around  $0.27\ \text{mol}\cdot\text{L}^{-1}$ ), allows to conclude that such polynuclear Al species were certainly involved in the processes occurring in the impregnation solution and leading to the deposition of bayerite on AC surface.

In the formation of the various  $\text{Al}(\text{OH})_3$  polymorphs, it has been suggested that the aforesaid polymeric Al species grow and, as a result of their interaction, a precipitate is finally developed. Specifically, the six-membered ring complex with composition  $[\text{Al}_6(\text{OH})_{12}(\text{H}_2\text{O})_{12}]^{6+}$  has been postulated as the precursor Al polymer in the crystallization of bayerite.<sup>[60]</sup> At this point, it is worth mentioning that the precipitation of bayerite from an  $\text{Al}(\text{NO}_3)_3$  aqueous solution with ammonia has been reported to begin at  $\text{pH} \sim 7$  and extend up to  $\text{pH} \sim 11$ .<sup>[61]</sup> This range should presumably comprise the pH value of the  $\text{Al}^{3+}$  impregnation solution just after its contact with AC during the preparation of the composite A120. Finally, bayerite was also reported to be the most stable  $\text{Al}(\text{OH})_3$  polymorph in alkaline solutions, thus supporting its presence in the A120 composite.<sup>[62]</sup>

**F120.** Selected SEM images for the composite F120 are gathered in Figure 3. At first sight, by comparing Figures 1a and 3a, no relevant morphological modifications in the surface of the raw AC are visualized upon its impregnation with  $\text{Fe}(\text{NO}_3)_3$  aqueous solution and subsequent oven-drying at  $120^\circ\text{C}$ . Likely, the only noticeable change is a slight increase in brightness for the external surface of F120. These observations are suggestive of the formation of highly dispersed iron phases covering almost the entire carbon surface, well in agreement with the results previously reported for other activated carbon-iron oxide composites prepared from the same commercial AC and iron oxide precursor under similar conditions as in the present work.<sup>[63,64]</sup> Furthermore, the aforesaid surface morphological features for F120 are also compatible with the formation and growth of the iron-containing phases mainly

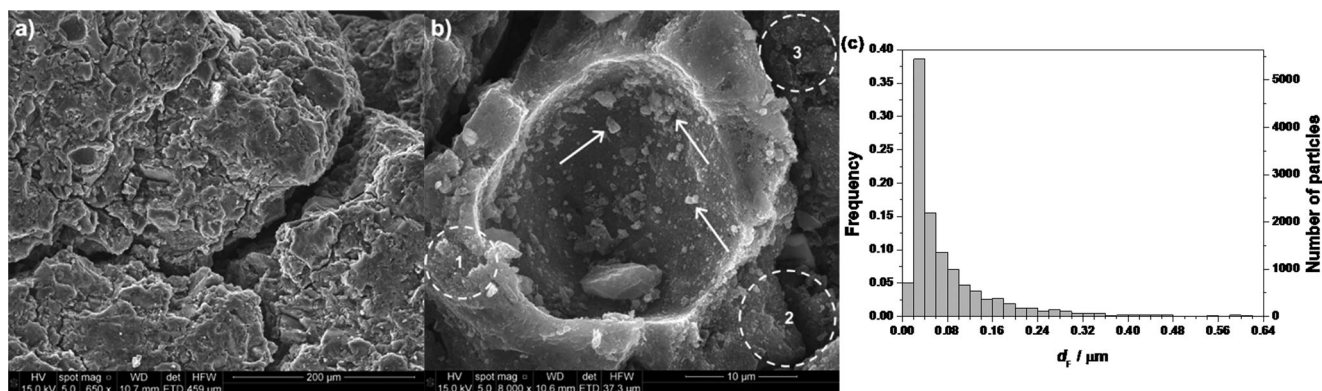
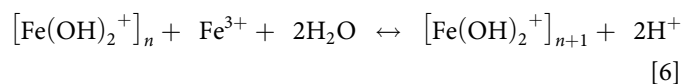


Figure 3. Selected SEM images ((a) and (b)) and PSD (c) for the composite F120.

inside the porous network of the AC substrate, leading to a certain porosity blockage and hence to a reduction of surface area.<sup>[49]</sup> Detailed examination of the higher magnification image in Figure 3b corroborates the presence of a high concentration of brighter particles evenly distributed over the outer surface of the carbon matrix. These particles exhibit a wide range of sizes, from very fine and uniform particles with nanometric dimensions (as those in the regions labeled as 1, 2 and 3 in Figure 3b) up to large aggregates in the microscale (arrowed in Figure 3b). Based on the measurements of a number of particles large enough (i.e. around 14,000 particles, see Table 3) in random regions of the sample external surface, the PSD for F120 has been estimated, and it is illustrated in Figure 3c. From this histogram, it follows that the particles show a very narrow size distribution, with predominance of those having nanometric dimensions (i.e. below 100 nm in size) and an average Feret's diameter of around 81.7 nm. XRD pattern for sample F120 (see Figure S2) indicates that these iron particles are only composed of goethite ( $\alpha$ -FeO(OH), orthorhombic system, space group *Pbnm*) with a tiny crystallite size of around 2.32 nm, thus revealing its essentially amorphous nature. This finding confirms that even the smaller supported particles seen in the F120 micrographs consist of clusters or aggregates of such extremely small goethite crystallites. The high degree of dispersion for the supported nanoparticles is likely connected not only with the large surface area and well-developed porosity of the carbon substrate but also with the high amount and variety of oxygen functional groups and structures on AC surface, as previously revealed by FT-IR spectroscopy.<sup>[54]</sup> In this regard, it should be kept in mind the great affinity of the Fe<sup>3+</sup> species in aqueous solution towards oxygen surface complexes, especially those acidic in character.<sup>[65]</sup> Accordingly, the introduction of oxygen functionalities on the surface of activated carbons by oxidation results in an increase of the adsorption of the iron precursor and, thereby, in an improvement of the dispersion of the resulting iron phase after the subsequent heat treatment.<sup>[66,67]</sup> As evidenced by our recent work using FT-IR and XPS spectroscopies,<sup>[68]</sup> the low pH value of the Fe(NO<sub>3</sub>)<sub>3</sub> impregnation aqueous solution employed in the present study (i.e. 1.54) significantly increases the oxidizing power of the NO<sub>3</sub><sup>-</sup> ions in such solution toward AC, thus creating new acidic

surface oxygen groups which behave as additional anchorage sites for the Fe<sup>3+</sup> species in solution.

As far as the chemistry of the iron precursor is concerned, chemical species such as the octahedral complex [Fe(H<sub>2</sub>O)<sub>6</sub>]<sup>3+</sup>, its hydrolysis products [Fe(H<sub>2</sub>O)<sub>5</sub>(OH)]<sup>2+</sup> and [Fe(H<sub>2</sub>O)<sub>4</sub>(OH)<sub>2</sub>]<sup>+</sup>, and the condensation products [Fe<sub>2</sub>(H<sub>2</sub>O)<sub>8</sub>(OH)<sub>2</sub>]<sup>4+</sup> and [Fe<sub>3</sub>(H<sub>2</sub>O)<sub>10</sub>(OH)<sub>4</sub>]<sup>5+</sup> have been identified in Fe(NO<sub>3</sub>)<sub>3</sub> aqueous solutions at pH values below 4.<sup>[69,70]</sup> From these solutions, precipitation of goethite slowly (from days to weeks) occurs through the following pathway: (i) formation of low molecular mass species, (ii) formation of a red cationic hydrolytic polymer, (iii) aging of this polymer, and (iv) precipitation of goethite. The proposed mechanisms for the formation and aging of the hydrolytic polymer entail condensation of [Fe(H<sub>2</sub>O)<sub>6-n</sub>(OH)<sub>n</sub>]<sup>(3-n)+</sup> species to give polymers in which Fe<sup>3+</sup> cations are bridged by OH<sup>-</sup> groups (olation, Equation (6)) or O<sup>2-</sup> anions (oxolation, Equation (7)).<sup>[69,71]</sup>



Similarly to the preparation of A120, the increase in the pH of the Fe(NO<sub>3</sub>)<sub>3</sub> impregnation solution after its contact with the AC support drastically alters the hydrolysis equilibria involving Fe<sup>3+</sup> species, and favors the precipitation of goethite. In addition, the high ionic strength of the impregnation solution, mainly ascribable to the NO<sub>3</sub><sup>-</sup> ions, has also been reported to accelerate the precipitation rate of goethite.<sup>[69]</sup> Nonetheless, it should be also pointed out that some investigations on the hydrolysis of Fe<sup>3+</sup> in nitrate solutions at high temperatures up to 90 °C have revealed that the lifetime of the aforementioned hydrolytic polymer decreases with increasing temperature.<sup>[71]</sup> Consequently, at the temperature of 80 °C used in the wet impregnation treatment, it is plausible that the formation of the intermediate polymer was scarce or even negligible.

Finally, it is worth highlighting that the very small size in the nanoscale of most goethite particles, together with their homogeneous distribution over the AC matrix, are both desirable characteristics with regard to the application of the composite F120 in catalytic and photocatalytic processes.

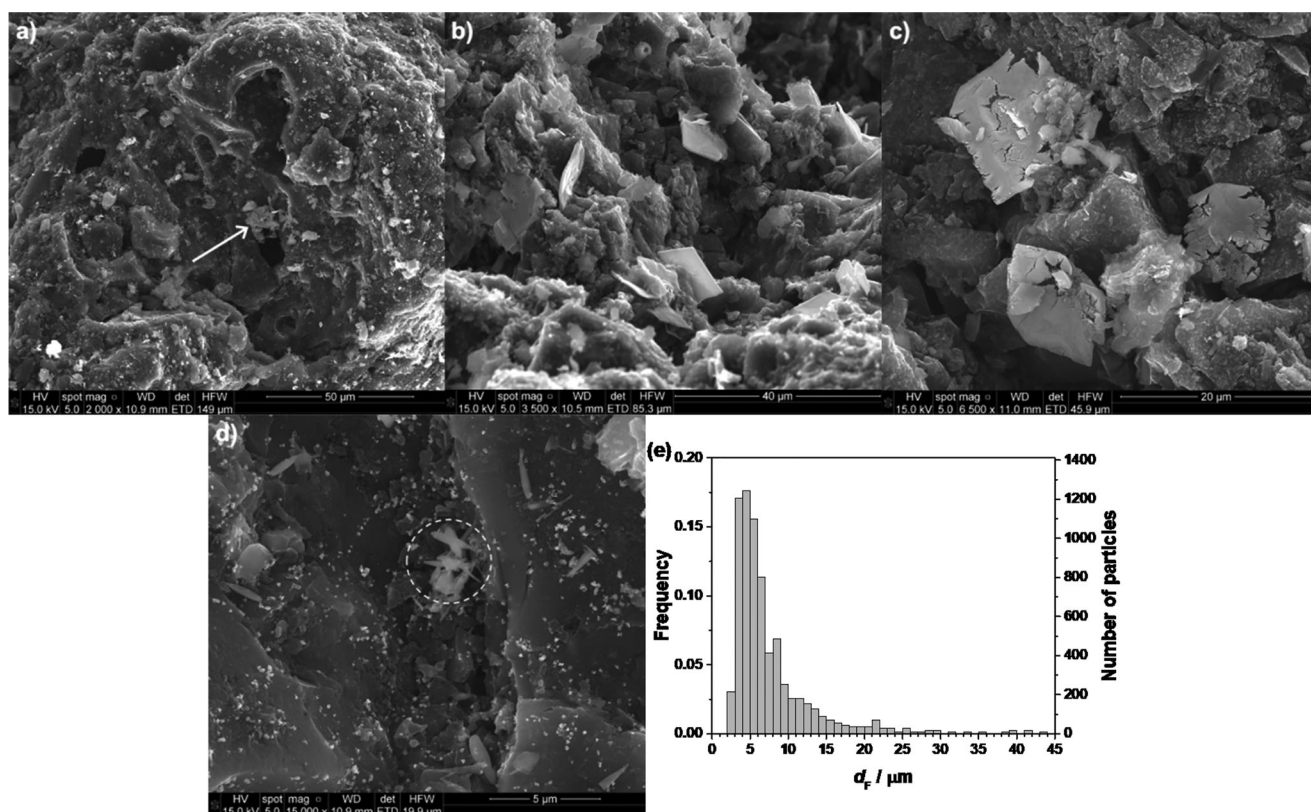


**Figure 4.** Selected SEM images ((a), (b), (c) and (d)) and PSD (e) for Z120.

**Z120.** Selected SEM images registered at different magnification levels for the composite Z120 are depicted in Figure 4. Upon impregnation of AC with  $\text{Zn}(\text{NO}_3)_2$  aqueous solution and successive oven-drying at  $120^\circ\text{C}$ , the formation of a heterogeneous coverage of well-dispersed brighter particles over the entire external surface of the AC grains is clearly seen in Figure 4a. In addition to very small isolated particles with nanometric dimensions, some regions covered by clusters of larger particles in the scale of micrometers, such as those arrowed in the above figure, are also seen. These observations seem to be in accordance with the morphological features previously described for several activated carbon-ZnO composites prepared by precipitation of  $\text{Zn}^{2+}$  in an aqueous solution of the nitrate salt with NaOH onto the carbon substrate and successive calcination at  $150^\circ\text{C}$ ,<sup>[72]</sup> and by simply mixing the activated carbon with an aqueous suspension of commercial ZnO powder.<sup>[73,74]</sup> The more homogeneous coverage for these latter samples is accounted for by the much greater ZnO content employed in their preparation. The XRD pattern for Z120 (see Figure S3) reveals that the supported particles mostly consist of  $\text{Zn}(\text{OH})_2$  adopting the crystalline structure of wülfingite ( $\epsilon$ - $\text{Zn}(\text{OH})_2$ , orthorhombic system, space group  $P2_12_12_1$ ), the most stable  $\text{Zn}(\text{OH})_2$  polymorph,<sup>[75]</sup> together with small amounts of ZnO grown in the zincite structure (hexagonal system, space group  $P6_3mc$ ). Wülfingite is likely supported on AC surface by precipitation from the  $\text{Zn}(\text{NO}_3)_2$  aqueous solution during the soaking step. This precursor solution had an initial pH value of around 5.16, which should have readily increased upon contact with the carbon substrate because of its basic character ( $\text{pH}_{\text{pzc}} = 10.50$ ) conferred by the presence on its surface of oxygen

functionalities, like pyrone and chromene type structures, as previously proved by FT-IR spectroscopy.<sup>[54]</sup> According to the speciation diagram for  $\text{Zn}^{2+}$  aqueous solutions,<sup>[76]</sup> the predominant chemical species in the impregnation solution under the starting conditions of pH and concentration is the aquo-complex  $[\text{Zn}(\text{H}_2\text{O})_4]^{2+}$ . Once the pH of the solution reaches the neutral region as a result of the contact with AC, the precipitation of  $\text{Zn}^{2+}$  as  $\text{Zn}(\text{OH})_2$  commences. As the wülfingite phase is only precipitated very slowly from aqueous medium, it may be assumed that this  $\text{Zn}(\text{OH})_2$  modification is formed by transformation of other less stable polymorphs under the mother liquor or even of the amorphous solid, which is always obtained when  $\text{Zn}^{2+}$  salt solutions, especially those prepared from  $\text{Zn}(\text{NO}_3)_2$ , are slightly alkalinized.<sup>[75]</sup> Obviously, the early stages of the subsequent oven-drying at  $120^\circ\text{C}$  may also contribute to accelerate such transformations. On the other hand, zincite is directly obtained from wülfingite by a partial thermal decomposition during the oven-drying step. In this regard, it has been reported that

**Table 4.** X-EDS compositional analyses on AC and the prepared AC-MO composites.

Sample	Spectrum	Carbon/wt.%	Oxygen/wt.%	O/C	Metal/wt.%
AC	1–3	86.69	6.32	0.07	—
A120	1	80.40	11.31	0.14	4.34
	2	80.97	11.98	0.15	3.70
	3	81.50	11.54	0.14	3.78
F120	1	60.41	15.26	0.25	19.41
	2	41.80	16.37	0.39	36.58
	3	41.57	9.98	0.24	42.87
Z120	1	80.95	10.70	0.13	4.38
	2	75.65	10.70	0.14	9.41
	3	75.28	9.35	0.12	7.97



the decomposition reaction of the different  $\text{Zn}(\text{OH})_2$  polymorphs occurs in the range from 70 to 140 °C, and the temperature is higher for the most stable wülfingite,<sup>[77]</sup> which explains the detection mostly of this phase in the Z120 composite after heating at 120 °C for 24 h.

Unlike the very irregular shape and essentially amorphous nature observed both for the bayerite and goethite particles in samples A120 and F120, respectively, closer inspection of the Z120 surface allows to identify several well-defined and markedly different morphologies for the supported particles. First, some of them display a morphology consisting of nearly rectangular and squared sheets of variable side length in the microscale, more or less sharp edges and relatively low thickness, as clearly seen in Figure 4b. The habit of such microcrystalline plates argues for a layered structure typical of wülfingite. The surface of these sheets is as a rule quite smooth, although some of them exhibit cracks and fissures, likely owing to the partial thermal decomposition, as well as serrated edges (see Figure 4c). Furthermore, one observes that these particles also tend to form aggregates of sheets and needles of different sizes and intersecting at variable angles, such as those circled in Figure 4d. In addition to the aforesaid structures, highly dispersed nanoparticles appearing as tiny white spots (see Figure 4d) are evenly dispersed over the darker outer surface of AC. Such spots are expected to be zincite nuclei with about 100 nm in size, quite similar to those previously reported for other activated carbon-ZnO/ $\text{Zn}(\text{OH})_2$  composites.<sup>[78]</sup> These results suggest that each large wülfingite crystal does not convert into a single ZnO crystal, but rather the conversion causes the wülfingite crystals to break up into smaller ones, which then break up once again into nanometer-sized ZnO crystals.<sup>[79]</sup> This behavior may be accounted for the great difference in density between wülfingite and zincite (i.e. 3.1 and 5.6 g·cm<sup>-3</sup>, respectively<sup>[79]</sup>). Finally, crystallite sizes estimated from XRD pattern corroborate the high degree of crystallinity both for wülfingite and zincite, having average sizes of 29.90 and 60.02 nm, respectively.

### X-EDS analysis

The different metal phases supported on AC are considered to have a predominant influence on the surface chemistry of the prepared hybrid materials. Because of the relatively high content and reactivity of these inorganic phases, it is evident that the chemical nature of the surface of the hybrid materials is not amenable to analysis by using traditional titration methods. X-EDS analyses were performed at selected areas of the samples in order to shed some light about the surface elemental composition of AC and each hybrid material and, thereby, about the dispersion both of metal and oxygen atoms. The resulting X-EDS spectra are illustrated in Figures S4–S7, and the corresponding quantification data as well as the oxygen to carbon ratios are summarized in Table 4.

The X-EDS spectra registered for the raw AC at three different locations (see Figure S4) are rather similarly featured as far as the number, position and intensity of peaks are concerned, so that it may be concluded that the elemental composition of the AC surface is very homogeneous. As

expected, these spectra display a very sharp and intense peak at around 0.29 keV attributable to carbon (i.e. the main constituent of AC), together with other much smaller peaks indicating the presence of heteroatoms such as oxygen and sulfur coming from the precursor material and/or the activating agent, which ultimately determine the surface chemistry of AC.<sup>[45]</sup> These heteroatoms are bonded to the carbon skeleton and form surface functional groups and structures analogous to those found in aromatic compounds, thereby reacting in a similar way with many reagents and being then differentiated in terms of their chemical reactivity. It should be noted that no nitrogen peak was observed in the aforesaid spectra, even though this heteroatom is also found in AC as revealed by elemental analysis (nitrogen content: 0.26 wt.%<sup>[80]</sup>). This fact is not surprising since it has been reported that for carbonaceous materials the nitrogen signal ( $\sim 0.39$  keV) is usually hidden by that of carbon, being only detected when an exceptionally high nitrogen concentration is present in the sample surface.<sup>[81]</sup> X-EDS results also reveal a relatively high silicon content (i.e.  $\sim 2.76$  wt.%) in AC surface, well in agreement with the XRD analysis, along with traces of other metal elements such as aluminum, iron and potassium, likely as a result of the inorganic matter contained in the precursor material.<sup>[50]</sup> Furthermore, the average oxygen content in the AC surface estimated from the three recorded X-EDS spectra (i.e. 6.32 wt.%) is markedly lower than that obtained for the bulk carbon sample by elemental analysis (i.e. 7.37 wt.%<sup>[45]</sup>), while the average carbon content values provided by both techniques are quite similar (86.50 and 86.69 wt.%), thus suggesting a certain preference of oxygen towards the formation of complexes on the walls of smaller pores rather than on the external surface of AC.

For the prepared hybrid materials, as compared to the pristine AC, the carbon content significantly decreases, while the oxygen content as a rule increases. Lower carbon contents are expected because of the decreased presence of carbonaceous material in the composite samples. Moreover, the increase in the oxygen contents may be related to contributions from the metal (hydr)oxide precursor and from the carbon-oxygen surface complexes formed during the impregnation and oven-drying treatments in the process of preparation of the composites. In this regard, coordination water and hydroxyl groups belonging to the coordination sphere of the metal cation precursors or to hydroxylated metal oxides should increase the oxygen content in the samples. Thus, the lower oxygen content for Z120 as compared to those for A120 and F120 can be explained on the basis of the smaller degree of hydroxylation of the  $\text{Zn}^{2+}$  ion than of the  $\text{Al}^{3+}$  and  $\text{Fe}^{3+}$  ions, as expected from their ion charges and sizes. In connection with the changes observed in the surface chemical composition of the raw AC after its impregnation with the aqueous solutions of the metal ion precursors, it should be kept in mind that they were prepared from nitrate salts and that their pH values were acidic as a result of the hydrolysis of the metal ions. The nitrate ion in such acidified aqueous solutions is well-known to behave as a strong oxidizing agent, being able to oxidize the

carbon surface and thus influencing as last resort most of the changes originated in the surface chemistry of AC.

## Conclusions

Using a granular commercial AC and  $\text{Al}(\text{NO}_3)_3$ ,  $\text{Fe}(\text{NO}_3)_3$  and  $\text{Zn}(\text{NO}_3)_2$  in aqueous solution as metal (hydr)oxide precursors, the surface microstructure, morphology and elemental chemical composition of the resulting composites prepared by wet impregnation at 80 °C for 5 h and oven-drying at 120 °C for 24 h are investigated by XRD, SEM and X-EDS. From the obtained results, the following main conclusions may be drawn. The morphological features of the composites, such as the crystalline habit, shape, size distribution and degree of dispersion of the supported particles, ultimately depend on the chemical changes undergone by the different precursor species not only in the impregnation solution after its contact with the AC substrate, but also during the subsequent oven-drying step (i.e. hydrolysis, polymerization and precipitation reactions, as well as thermal ageing). As a result of the increase of pH in the impregnation solution because of the basic character of AC, the complex hydrolysis and polymerization processes involving  $\text{Al}^{3+}$ ,  $\text{Fe}^{3+}$  and  $\text{Zn}^{2+}$  species are strongly affected, thus leading to the precipitation of the corresponding metal hydroxides or oxyhydroxides. Both supported bayerite and goethite are essentially amorphous in nature; however, the former grows in micrometric particles while the latter does mainly as nanoparticles. By contrast, the higher crystallinity degree and larger particle size observed for the supported wulfingite are connected with the transformation of the amorphous phase during the heating at 120 °C. Finally, the combination of SEM and ImageJ processing program has enabled to assess the PSD of AC-MO composites in an accurate, quick and reproducible way, thus overcoming the drawbacks inherent to other widely employed techniques, such as physisorption/chemisorption of selected gases and vapors and X-ray diffraction.

## Acknowledgements

Financial support by Junta de Extremadura and European FEDER Funds is gratefully acknowledged. Adrián Barroso-Bogeat thanks support from the “Juan de la Cierva-Formación” Fellowship Program of Spanish Ministry of Science, Innovation and Universities (FJCI-2015-25999).

## ORCID

Adrián Barroso-Bogeat  <https://orcid.org/0000-0002-1272-3834>

## References

- [1] Barroso-Bogeat, A.; Alexandre-Franco, M.; Fernández-González, C.; Sánchez-González, J.; Gómez-Serrano, V. Electrical Conductivity of Metal (Hydr)Oxide-Activated Carbon Composites under Compression. A Comparison Study. *Mater. Chem. Phys. [Internet]* **2015**, *152*, 113–122. <http://www.scopus.com/inward/record.url?eid=2-s2.0-84920279945&partnerID=tZotx3y1>. DOI: 10.1016/j.matchemphys.2014.12.022.
- [2] Ehrburger, P. Dispersion of Small Particles on Carbon Surfaces. *Adv. Colloid Interface Sci.* **1984**, *21*, 275–302. DOI: 10.1016/0001-8686(84)85002-2.
- [3] Cameron, D. S.; Cooper, S. J.; Dodgson, I. L.; Harrison, B.; Jenkins, J. W. Carbons as Supports for Precious Metal Catalysts. *Catal. Today* **1990**, *7*, 113–137. DOI: 10.1016/0920-5861(90)85012-D.
- [4] Radovic, L. R.; Rodríguez-Reinoso, F. Carbon Materials in Catalysis. In *Chemistry & Physics of Carbon*; Thrower PA, Ed.; Marcel Dekker: New York, **1996**; Vol. 25, pp 243–358.
- [5] Rodríguez-Reinoso, F. The Role of Carbon Materials in Heterogeneous Catalysis. *Carbon N. Y* **1998**, *36*, 159–175. DOI: 10.1016/S0008-6223(97)00173-5.
- [6] Furimsky, E. *Carbons and Carbon Supported Catalysts in Hydroprocessing*; Royal Society of Chemistry: Cambridge, **2008**.
- [7] Serp, P.; Figueiredo, J. L. *Carbon Materials for Catalysis*; John Wiley & Sons: Hoboken, **2009**.
- [8] Goyal M. Nonenvironmental Industrial Applications of Activated Carbon Adsorption. In *Novel Carbon Adsorbents*; Tascón, J. M. D., Ed.; Elsevier: Amsterdam, **2012**; pp 605–638.
- [9] Barroso-Bogeat, A.; Fernández-González, C.; Alexandre-Franco, M. Activated Carbon as a Metal Oxide Support: A Review. In *Activated Carbon: Classifications, Properties and Applications*, Kwiatkowski, J. F., Ed.; Nova Science Publishers: New York, **2012**; pp 297–318.
- [10] Serp, P.; Machado, B. *Nanostructured Carbon Materials for Catalysis*; Royal Society of Chemistry: Cambridge, **2015**.
- [11] Jüntgen, H. Activated Carbon as Catalyst Support. A Review of New Research Results. *Fuel* **1986**, *65*, 1436–1446. DOI: 10.1016/0016-2361(86)90120-1.
- [12] Wang, S.; (Max)Lu, G. Q. Effects of Acidic Treatments on the Pore and Surface Properties of Ni Catalyst Supported on Activated Carbon. *Carbon N. Y. [Internet]* **1998**, *36*, 283–292. <http://linkinghub.elsevier.com/retrieve/pii/S0008622397001875>. DOI: 10.1016/S0008-6223(97)00187-5.
- [13] Rodríguez-Reinoso, F.; Sepúlveda-Escribano, A. Carbon as Catalyst Support. In *Carbon Materials in Catalysis*; Serp, P.; Figueiredo, J. L., Ed.; John Wiley & Sons: Hoboken, **2009**; pp 131–155.
- [14] Derbyshire, F. J.; de Beer, V. H. J.; Abotsi, G. M. K.; Scaroni, A. W.; Solar, J. M.; Skrovanek, D. J. The Influence of Surface Functionality on the Activity of Carbon-Supported Catalysts. *Appl. Catal.* **1986**, *27*, 117–131. DOI: 10.1016/S0166-9834(00)81051-9.
- [15] Jin Suh, D.; Tae-Jin, P.; Ihm, S.-K. Effect of Surface Oxygen Groups of Carbon Supports on the Characteristics of Pd/C Catalysts. *Carbon N. Y.* **1993**, *31*, 427–435.
- [16] Román-Martínez, M. C.; Cazorla-Amorós, D.; Linares-Solano, A.; De Lecea, C. S.-M.; Yamashita, H.; Anpo, M. Metal-Support Interaction in Pt/C Catalysts. Influence of the Support Surface Chemistry and the Metal Precursor. *Carbon N. Y.* **1995**, *33*, 3–13. DOI: 10.1016/0008-6223(94)00096-I.
- [17] Tseng, H.-H.; Wey, M.-Y. Study of SO<sub>2</sub> Adsorption and Thermal Regeneration over Activated Carbon-Supported Copper Oxide Catalysts. *Carbon N. Y.* **2004**, *42*, 2269–2278. DOI: 10.1016/j.carbon.2004.05.004.
- [18] Arunajatesan, V.; Chen, B.; Möbus, K. Carbon-Supported Catalysts for the Chemical Industry. In *Carbon Materials in Catalysis*; Serp, P.; Figueiredo, J. L., Ed.; John Wiley & Sons: Hoboken, **2009**; pp 535–572.
- [19] Yang, Y.; Chiang, K.; Burke, N. Porous Carbon-Supported Catalysts for Energy and Environmental Applications: A Short Review. *Catal. Today [Internet]* **2011**, *178*, 197–205. DOI: 10.1016/j.cattod.2011.08.028.
- [20] Prado-Burguete, C.; Linares-Solano, A.; Rodríguez-Reinoso, F.; Salinas-Martínez de Lecea, C. The Effect of Oxygen Surface Groups of the Support on Platinum Dispersion in Pt/Carbon Catalysts. *J. Catal.* **1989**, *115*, 98–106.
- [21] Prado-Burguete, C.; Linares-Solano, A.; Rodríguez-Reinoso, F.; Salinas-Martínez de Lecea, C. Effect of Carbon Support and

- Mean Pt Particle Size on Hydrogen Chemisorption by Carbon-Supported Pt Catalysts. *J. Catal.* **1991**, *128*, 397–404.
- [22] Bitter, J. H.; de Jong, K. P. Preparation of Carbon-Supported Metal Catalysts. In *Carbon Materials in Catalysis*; Serp, P.; Figueiredo, J. L., Ed.; John Wiley & Sons: Hoboken, **2009**; pp 157–176.
- [23] Han, W.; Liu, H.; Zhu, H. Effect of Activated Carbon on the Dispersion of Ru and K over Supported Ru-Based Catalyst for Ammonia Synthesis. *Catal. Commun.* **2007**, *8*, 351–354. DOI: [10.1016/j.catcom.2006.07.006](https://doi.org/10.1016/j.catcom.2006.07.006).
- [24] Ma, W.; Kugler, E. L.; Dadyburjor, D. B. Effect of Properties of Various Activated-Carbon Supports and Supported Fe-Mo-Cu-K Catalysts on Metal Precursor Distribution, Metal Reduction, and Fischer-Tropsch Synthesis. *Energy Fuels* **2010**, *24*, 4099–4110. DOI: [10.1021/ef1003107](https://doi.org/10.1021/ef1003107).
- [25] Yang, F.; Deng, D.; Pan, X.; Fu, Q.; Bao, X. Understanding Nano Effects in Catalysis. *Nat. Sci. Rev.* **2015**, *2*, 183–201.
- [26] Luss, D. The Effect of Crystallite Size Distribution on Specific Activity of Supported Catalysts. *J. Catal.* **1971**, *23*, 119–123. DOI: [10.1016/0021-9517\(71\)90031-5](https://doi.org/10.1016/0021-9517(71)90031-5).
- [27] Mastikhin, V. M.; Goncharova, S. N.; Tapilin, V. M.; Terskikh, V. V.; Balzhinimaev, B. S. Effect of Particle Size upon Catalytic and Electronic Properties of Supported Ag Catalysts: Combined Catalytic, 109Ag NMR and Quantum Chemistry Studies. *J. Mol. Catal. A Chem. [Internet]* **1995**, *96*, 175–179. <http://linkinghub.elsevier.com/retrieve/pii/1381116994000190>. DOI: [10.1016/1381-1169\(94\)00019-0](https://doi.org/10.1016/1381-1169(94)00019-0).
- [28] Maillard, F.; Eikerling, M.; Cherstiouk, O. V.; Schreier, S.; Savinova, E.; Stimming, U. Size Effects on Reactivity of Pt Nanoparticles in CO Monolayer Oxidation: The Role of Surface Mobility. *Faraday Discuss.* **2004**, *125*, 357–377.
- [29] Bezemer, G. L.; Bitter, J. H.; Kuipers, H. P. C. E.; Oosterbeek, H.; Holewijn, J. E.; Xu, X.; Kapteijn, F.; van Dillen, A. J.; de Jong, K. P. Cobalt Particle Size Effects in the Fischer-Tropsch Reaction Studied with Carbon Nanofiber Supported Catalysts. *J. Am. Chem. Soc.* **2006**, *128*, 3956–3964. DOI: [10.1021/ja058282w](https://doi.org/10.1021/ja058282w).
- [30] Godoi, D. R. M.; Perez, J.; Villullas, H. M. Influence of Particle Size on the Properties of Pt–Ru/C Catalysts Prepared by a Microemulsion Method. *J. Electrochem. Soc.* **2007**, *154*, B474–B479. <http://jes.ecsdl.org/cgi/doi/10.1149/1.2713689>. DOI: [10.1149/1.2713689](https://doi.org/10.1149/1.2713689).
- [31] Perez, J.; Paganin, V. A.; Antolini, E. Particle Size Effect for Ethanol Electro-Oxidation on Pt/C Catalysts in Half-Cell and in a Single Direct Ethanol Fuel Cell. *J. Electroanal. Chem. [Internet]* **2011**, *654*, 108–115. DOI: [10.1016/j.jelechem.2011.01.013](https://doi.org/10.1016/j.jelechem.2011.01.013).
- [32] Rozanska, X.; Fortrie, R.; Sauer, J. Size-Dependent Catalytic Activity of Supported Vanadium Oxide Species: Oxidative Dehydrogenation of Propane. *J. Am. Chem. Soc.* **2014**, *136*, 7751–7761. DOI: [10.1021/ja503130z](https://doi.org/10.1021/ja503130z).
- [33] Whyte, T. E. Metal Particle Size Determination of Supported Metal Catalysts. *Catal. Rev. Sci. Eng.* **1974**, *8*, 117–134. DOI: [10.1080/01614947408071858](https://doi.org/10.1080/01614947408071858).
- [34] Chaturvedi, S.; Dave, P. N. Electron Microscopy in Heterogeneous Catalysis. In *Microscopy: Science, Technology, Applications and Education*; Méndez-Vilas, A., Ed.; Formatex: Badajoz, **2014**; pp 813–818.
- [35] Barroso-Bogeat, A.; Alexandre-Franco, M.; Fernández-González, C.; Gómez-Serrano, V. Preparation and Microstructural Characterization of Activated Carbon-Metal Oxide Hybrid Catalysts: New Insights into Reaction Paths. *J. Mater. Sci. Technol. [Internet]* **2015**, *31*, 806–814. <http://linkinghub.elsevier.com/retrieve/pii/S1005030215000985>. DOI: [10.1016/j.jmst.2015.06.004](https://doi.org/10.1016/j.jmst.2015.06.004).
- [36] Barroso-Bogeat, A.; Alexandre-Franco, M.; Fernández-González, C.; Gómez-Serrano, V. Preparation of Activated Carbon-Metal (Hydr)Oxide Materials by Thermal Methods. Thermogravimetric-Mass Spectrometric (TG-MS) Analysis. *J. Anal. Appl. Pyrolysis [Internet]* **2015**, *116*, 243–252. <http://linkinghub.elsevier.com/retrieve/pii/S0165237015301789>. DOI: [10.1016/j.jaap.2015.09.004](https://doi.org/10.1016/j.jaap.2015.09.004).
- [37] Barroso-Bogeat, A.; Alexandre-Franco, M.; Fernández-González, C. Physico-Chemical Characterization of Activated Carbon–Metal Oxide Photocatalysts by Immersion Calorimetry in Benzene and Water. *J. Therm. Anal. Calorim. [Internet]* **2016**, *125*, 65–74. <http://link.springer.com/10.1007/s10973-016-5337-6>.
- [38] Standard ISO 13322-1. Particle Size Analysis – Image Analysis Methods – Part 1: Static Image Analysis Methods. **2014**.
- [39] Rasband, W. S. *ImageJ*; U.S. National Institute of Health: Bethesda, **1997**.
- [40] Mazzoli, A.; Favoni, O. Particle Size, Size Distribution and Morphological Evaluation of Airborne Dust Particles of Diverse Woods by Scanning Electron Microscopy and Image Processing Program. *Powder Technol. [Internet]* **2012**, *225*, 65–71. DOI: [10.1016/j.powtec.2012.03.033](https://doi.org/10.1016/j.powtec.2012.03.033).
- [41] Mazzoli, A.; Moriconi, G. Particle Size, Size Distribution and Morphological Evaluation of Glass Fiber Reinforced Plastic (GRP) Industrial by-Product. *Micron [Internet]* **2014**, *67*, 169–178. DOI: [10.1016/j.micron.2014.07.007](https://doi.org/10.1016/j.micron.2014.07.007).
- [42] Barroso-Bogeat, A.; Alexandre-Franco, M.; Fernández-González, C.; Gómez-Serrano, V. Particle Size Distribution and Morphological Changes in Activated Carbon-Metal Oxide Hybrid Catalysts Prepared under Different. *J. Microsc. [Internet]* **2016**, *261*, 227–242. <http://doi.wiley.com/10.1111/jmi.12323>. DOI: [10.1111/jmi.12323](https://doi.org/10.1111/jmi.12323).
- [43] Hýtch, M. J.; Gandais, M. Quantitative Criteria for the Detection and Characterization of Nanocrystals from High-Resolution Electron Microscopy Images. *Philos. Mag. A [Internet]* **1995**, *72*, 619–634. <http://www.tandfonline.com/doi/abs/10.1080/01418619508243789>. DOI: [10.1080/01418619508243789](https://doi.org/10.1080/01418619508243789).
- [44] Heinemann, K.; Soria, F. On the Detection and Size Classification of Nanometer-Size Metal Particles on Amorphous Substrates. *Ultramicroscopy [Internet]* **1986**, *20*, 1–14. <https://www.science-direct.com/science/article/abs/pii/0304399186901610>.
- [45] Bansal, R. C.; Donnet, J. B.; Stoeckli, F. *Active Carbon*; Marcel Dekker: New York, **1988**.
- [46] Marsh, H.; Rodríguez-Reinoso, F. *Activated Carbon*; Elsevier: Amsterdam, **2006**.
- [47] Achaw O-W. A Study of the Porosity of Activated Carbons Using the Scanning Electron Microscope. In *Scanning Electron Microscopy*; Kazmiruk, V., Ed.; InTech: London, **2002**; pp 472–490.
- [48] Achaw, O.-W.; Afrane, G. The Evolution of the Pore Structure of Coconut Shells during the Preparation of Coconut Shell-Based Activated Carbons. *Micropor. Mesopor. Mater.* **2008**, *112*, 284–290. DOI: [10.1016/j.micromeso.2007.10.001](https://doi.org/10.1016/j.micromeso.2007.10.001).
- [49] Barroso-Bogeat, A.; Alexandre-Franco, M.; Fernández-González, C.; Gómez-Serrano, V. Preparation of Activated Carbon-Metal Oxide Hybrid Catalysts: Textural Characterization. *Fuel Process. Technol.* **2014**, *126*, 95–103. DOI: [10.1016/j.fuproc.2014.04.022](https://doi.org/10.1016/j.fuproc.2014.04.022).
- [50] Matos, J.; Nahas, C.; Rojas, L.; Rosales, M. Synthesis and Characterization of Activated Carbon from Sawdust of Algarroba Wood. 1. Physical Activation and Pyrolysis. *J. Hazard. Mater. [Internet]* **2011**, *196*, 360–369. DOI: [10.1016/j.jhazmat.2011.09.046](https://doi.org/10.1016/j.jhazmat.2011.09.046).
- [51] Suárez-García, F.; Martínez-Alonso, A.; Fernández Llorente, M.; Tascón, J. M. D. Inorganic Matter Characterization in Vegetable Biomass Feedstocks. *Fuel* **2002**, *81*, 1161–1169.
- [52] Badosz, T. J.; Ania, C. O. Surface Chemistry of Activated Carbons and Its Characterization. In *Activated Carbon Surfaces in Environmental Remediation*; Badosz, T. J., Ed.; Elsevier: Amsterdam, **2006**; pp 159–229.
- [53] Antunes, M. L. P.; Santos, H.; de, S.; Santos, P.; de, S. Characterization of the Aluminum Hydroxide Microcrystals Formed in Some Alcohol-Water Solutions. *Mater. Chem. Phys.* **2002**, *76*, 243–249. DOI: [10.1016/S0254-0584\(01\)00535-1](https://doi.org/10.1016/S0254-0584(01)00535-1).

- [54] Barroso-Bogeat, A.; Alexandre-Franco, M.; Fernández-González, C.; Gómez-Serrano, V. FT-IR Analysis of Pyrone and Chromene Structures in Activated Carbon. *Energy Fuels* **2014**, *28*, 4096–4103. DOI: [10.1021/ef5004733](https://doi.org/10.1021/ef5004733).
- [55] Leon y Leon, C. A.; Solar, J. M.; Calemma, V.; Radovic, L. R. Evidence for the Protonation of Basal Plane Sites on Carbon. *Carbon N. Y.* **1992**, *30*, 797–811. DOI: [10.1016/0008-6223\(92\)90164-R](https://doi.org/10.1016/0008-6223(92)90164-R).
- [56] Bertsch, P. M.; Parker, D. R. Aqueous Polynuclear Aluminum Species. In *Environmental Chemistry of Aluminum*; Sposito, G., Ed.; Lewis Publishers: Boca Raton, **1996**; pp 117–168.
- [57] Martin, R. B. The Chemistry of Aluminum as Related to Biology and Medicine. *Clin. Chem.* **1986**, *32*, 1797–1806.
- [58] Lydersen, E.; Salbu, B.; Poleo, A. B. S. The Influences of Temperature on Aqueous Aluminium Chemistry. *Water. Air. Soil Pollut.* **1990**, *51*, 203–215.
- [59] Hem, J. D.; Roberson, C. E. *Form and Stability of Aluminum Hydroxide Complexes in Dilute Solution*; USGS Water Supply Pap: Washington, **1967**.
- [60] Hsu, P. H.; Bates, T. F. Formation of X-Ray Amorphous and Crystalline Aluminium Hydroxides. *Mineral. Mag. J. Mineral Soc.* **1964**, *33*, 749–768. DOI: [10.1180/minmag.1964.033.264.04](https://doi.org/10.1180/minmag.1964.033.264.04).
- [61] Du, X.; Wang, Y.; Su, X.; Li, J. Influences of pH Value on the Microstructure and Phase Transformation of Aluminium Hydroxide. *Powder Technol. [Internet]* **2009**, *192*, 40–46. DOI: [10.1016/j.powtec.2008.11.008](https://doi.org/10.1016/j.powtec.2008.11.008).
- [62] Raupach, M. Solubility of Simple Aluminium Compounds Expected in Soils. I. Hydroxides and Oxyhydroxides. *Soil Res.* **1963**, *1*, 28–35. DOI: [10.1017/SR9630028](https://doi.org/10.1017/SR9630028).
- [63] Castro, C. S.; Guerreiro, M. C.; Oliveira, L. C. A.; Gonçalves, M.; Anastácio, A. S.; Nazzarro, M. Iron Oxide Dispersed over Activated Carbon: Support Influence on the Oxidation of the Model Molecule Methylene Blue. *Appl. Catal. A Gen.* **2009**, *367*, 53–58. DOI: [10.1016/j.apcata.2009.07.032](https://doi.org/10.1016/j.apcata.2009.07.032).
- [64] Castro, C. S.; Oliveira, L. C. A.; Guerreiro, M. C. Effect of Hydrogen Treatment on the Catalytic Activity of Iron Oxide Based Materials Dispersed over Activated Carbon: Investigations toward Hydrogen Peroxide Decomposition. *Catal. Lett.* **2009**, *133*, 41–48. DOI: [10.1007/s10562-009-0167-9](https://doi.org/10.1007/s10562-009-0167-9).
- [65] Gu, Z.; Fang, J.; Deng, B. Preparation and Evaluation of GAC-Based Iron-Containing Adsorbents for Arsenic Removal. *Environ. Sci. Technol.* **2005**, *39*, 3833–3843. DOI: [10.1021/es048179r](https://doi.org/10.1021/es048179r).
- [66] Muñoz, G.; Fierro, V.; Celzard, A.; Furdin, G.; Gonzalez-Sánchez, G.; Ballinas, M. L. Synthesis, Characterization and Performance in Arsenic Removal of Iron-Doped Activated Carbons Prepared by Impregnation with Fe(III) and Fe(II). *J. Hazard. Mater.* **2009**, *165*, 893–902. DOI: [10.1016/j.jhazmat.2008.10.074](https://doi.org/10.1016/j.jhazmat.2008.10.074).
- [67] Fierro, V.; Muñoz, G.; Gonzalez-Sánchez, G.; Ballinas, M. L.; Celzard, A. Arsenic Removal by Iron-Doped Activated Carbons Prepared by Ferric Chloride Forced Hydrolysis. *J. Hazard. Mater.* **2009**, *168*, 430–437. DOI: [10.1016/j.jhazmat.2009.02.055](https://doi.org/10.1016/j.jhazmat.2009.02.055).
- [68] Barroso-Bogeat, A.; Alexandre-Franco, M.; Fernández-González, C.; Gómez-Serrano, V. Activated Carbon Surface Chemistry: Changes Upon Impregnation with Al(III), Fe(III) and Zn(II)-Metal Oxide Catalyst Precursors from NO<sub>3</sub>-Aqueous Solutions. *Arab. J. Chem.* **2016**. DOI: [10.1016/j.arabj.2016.02.018](https://doi.org/10.1016/j.arabj.2016.02.018).
- [69] Flynn, C. M. Hydrolysis of Inorganic Iron(III) Salts. *Chem. Rev.* **1984**, *84*, 31–41. DOI: [10.1021/cr00059a003](https://doi.org/10.1021/cr00059a003).
- [70] Lopes, L.; de Laat, J.; Legube, B. Charge Transfer of Iron(III) Monomeric and Oligomeric Aqua Hydroxo Complexes: Semiempirical Investigation into Photoactivity. *Inorg. Chem.* **2002**, *41*, 2505–2517.
- [71] Dousma, J.; de Bruyn, P. L. Hydrolysis-Precipitation Studies of Iron Solutions. *J. Colloid Interface Sci.* **1976**, *56*, 527–539. DOI: [10.1016/0021-9797\(76\)90119-3](https://doi.org/10.1016/0021-9797(76)90119-3).
- [72] Hernández, S. P.; Chiappero, M.; Russo, N.; Fino, D. A Novel ZnO-Based Adsorbent for Biogas Purification in H<sub>2</sub> Production Systems. *Chem. Eng. J.* **2011**, *176–177*, 272–279. DOI: [10.1016/j.cej.2011.06.085](https://doi.org/10.1016/j.cej.2011.06.085).
- [73] Sobana, N.; Swaminathan, M. Combination Effect of ZnO and Activated Carbon for Solar Assisted Photocatalytic Degradation of Direct Blue 53. *Sol. Energy Mater. Sol. Cells* **2007**, *91*, 727–734. DOI: [10.1016/j.solmat.2006.12.013](https://doi.org/10.1016/j.solmat.2006.12.013).
- [74] Sobana, N.; Muruganandam, M.; Swaminathan, M. Characterization of AC-ZnO Catalyst and Its Photocatalytic Activity on 4-Acetylphenol Degradation. *Catal. Commun.* **2008**, *9*, 262–268. DOI: [10.1016/j.catcom.2007.04.040](https://doi.org/10.1016/j.catcom.2007.04.040).
- [75] Oswald, H. R.; Asper, R. Bivalent Metal Hydroxides. In *Preparation and Crystal Growth of Materials with Layered Structures*; Lieth, R. M. A., Ed.; Kluwer Academic Publishers: Dordrecht, **1977**; pp. 71–140.
- [76] Carrott, P. J. M.; Carrott, M. M. L. R.; Nabais, J. M. V.; Ramalho, J. P. P. Influence of Surface Ionization on the Adsorption of Aqueous Zinc Species by Activated Carbons. *Carbon N. Y.* **1997**, *35*, 403–410. DOI: [10.1016/S0008-6223\(97\)89611-X](https://doi.org/10.1016/S0008-6223(97)89611-X).
- [77] Giovanoli, R.; Oswald, H. R.; Feitknecht, W. Über Die Thermische Zersetzung Der Kristallinen Zinkhydroxide. *Helv. Chim. Acta* **1966**, *49*, 1971–1983. DOI: [10.1002/hlca.660490704](https://doi.org/10.1002/hlca.660490704).
- [78] Mosayebi, E.; Azizian, S.; Hajian, A. Synthesis of Nanostructured and Microstructured ZnO and Zn(OH)<sub>2</sub> on Activated Carbon Cloth by Hydrothermal and Microwave-Assisted Chemical Bath Deposition Methods. *Superlattices Microstruct.* [Internet] **2015**, *81*, 226–232. <http://linkinghub.elsevier.com/retrieve/pii/S0749603615000543>. DOI: [10.1016/j.spmi.2014.12.039](https://doi.org/10.1016/j.spmi.2014.12.039).
- [79] Nicholas, N. J. *Control of ZnO Crystal Morphology Through Face Specific Adsorption*; University of Melbourne: Melbourne, **2011**.
- [80] Barroso-Bogeat, A. Preparation of Activated Carbon-Metal Oxide Hybrid Catalysts: Textural Characterization. *Fuel Process [Internet]* **2014**, *126*, 95–103. <http://www.sciencedirect.com/science/article/pii/S037838201400174X>.
- [81] Bagreev, A.; Angel Menendez, J.; Dukhno, I.; Tarasenko, Y.; Bandosz, T. J. Bituminous Coal-Based Activated Carbons Modified with Nitrogen as Adsorbents of Hydrogen Sulfide. *Carbon N. Y.* **2004**, *42*, 469–476. DOI: [10.1016/j.carbon.2003.10.042](https://doi.org/10.1016/j.carbon.2003.10.042).